Particle
& Particle Systems Characterization
www.particle-journal.com

High Catalytic Performance of Silver-Doped Gold Nanocages for Methanol Electrooxidation

Hongjun You, Lijun Zhao, Yun Zuo, and Jixiang Fang*

Hollow or porous noble metal nanocrystals with large specific electrochemical surface area and stability hold stimulating technological applications in fuel cell catalysis. Here, a simple galvanic replacement reaction synthesis of Ag-doped Au nanocages with a tunable Ag/Au atomic ratio is developed. Without surface ligands being used in the synthesis, the obtained AuAg nanocages with hollow cavity and opened nanoporous shell possess clean surface and enhanced electrocatalytic activity. In the electrocatalysis of the methanol oxidation reaction (MOR), the obtained AuAg nanocages possess high electrocatalysis properties and show morphology and composition-dependent electrocatalytic property. The optimized AuAg cubic nanocages that have 5% Ag exhibit excellent electrocatalytic activity for MOR, and this is attributed to the unique geometric structure and the well-controlled Ag content. The hollow and nanoporous structure can effectively promote the mass transfer and atomic utilization during the catalytic process for MOR. Density functional theory calculations indicate that introducing of a small amount of Ag facilitates methanol adsorption to the surface of catalysts and promotes the break of the O—H bond during the MOR process, thus accordingly enhances the catalytic activity.

1. Introduction

Because noble-metal nanocrystals are used in a broad range of applications, such as bioimaging, sensors, (electro)-catalysis, and drug delivery, their design and synthesis with rationally controlled nanostructures and functions have drawn enormous attention.[1–5] In the past, the influences of size, composition, shape, and crystalline structure of noble metals and their alloy nanocrystals on various application performance have been studied in detail, and the corresponding theories have been revealed in depth.[6–12] Recently, with goals of using noble metal nanocrystals in specific applications, people are intending to design novel nanocrystals coupling multiple merits of the composition, shape, nanostructure, and crystalline structure to obtain integrated high application properties.[13–17] Noble metal nanocrystals are important electrocatalysts for direct methanol fuel cells (DMFCs).[6,12,18–20] DMFCs have attracted great attention because methanol is a green energy source and owns many advantages such as easy synthesis, convenient transportation and storage, and high theoretical gravimetric and volumetric energy capacity.[21–23] Unfortunately, noble metal electrocatalysts are very expensive. Thus, people have devoted a great deal of effort to the design and synthesis of noble metal electrocatalysts that have excellent electrocatalytic activity for the methanol oxidation reaction (MOR).[14,23–26] To increase the utilization efficiency of noble metals, the basic strategy is to increase the proportion of atoms that are exposed on the surface by reducing the size of the noble metal nanoparticles.[27,28] Despite the extensive use of this strategy, it is still difficult to achieve excellent catalytic activity and stability through engineering the composition and surface structure of noble metal electrocatalysts. Ultrasmall nanoparticles are unstable in an electrocatalytic system. Under electronic potential, the nanoparticles tend to agglomerate and sinter (forming larger particles), detach from the support, or undergo both during an electrocatalytic process.[3,29] To overcome these issues, hollow or porous noble metal nanocrystals have gained stimulating research interest in electrocatalysis.

Various hollow or porous noble metal nanostructures have been fabricated using different methods, in which templating strategies are extensively used. The templates can be characterized as soft, hard, and sacrificial template. For example, nonsymmetrical Au and Ag/AgI nanoplates have been synthesized using 2D soft-templates;[30,31] uniform Pt, Au, and AuAg alloy porous nanostructures have been prepared using mesoporous silica or carbon as hard templates;[32–34] and Pt, Ag, and PtRhCu hollow nanoparticles have been constructed using Ag, Ag_2O, and Cu_2O nanoparticles as sacrificial templates.[15,23,35] These porous and hollow nanostructures have large specific surface areas and are desirable candidates for catalysts. In our previous study, hollow cubic Pt nanobox was synthesized using Ag

H. J. You, J. X. Fang
Key Laboratory of Biomedical Information Engineering of Ministry of Education
School of Life Science and Technology
Research Institute of Xi'an Jiaotong University, Zhejiang
Xi'an Jiaotong University
Xi'an, Shaanxi 710049, China
E-mail: hjyou@mail.xjtu.edu.cn
L. J. Zhao, Y. Zuo
MOE Key Laboratory for Non-equilibrium Synthesis and Modulation of Condensed Matter
School of Physics
Xi'an Jiaotong University
Shaanxi 710049, China
The ORCID identification number(s) for the author(s) of this article can be found under https://doi.org/10.1002/ppsc.202100248.

DOI: 10.1002/ppsc.202100248

nanoparticle as a sacrificial template, and the hollow structure performed excellent electrocatalytic activity for MOR.[36] Later, using octahedral Pd nanoparticles as a sacrificial template, Xia group constructed hollow octahedral PtPd nanocages with porous walls which show greatly enhanced electrocatalytic properties.[37] In our recent work, we further find that doping Ag obviously promotes the electocatalytic activity of porous Au nanocrystals.[34]

In this work, we use Cu_2O nanoparticle as a sacrificial template to design and synthesize hollow Ag-doped Au nanocages that have a clean surface. The morphology- and composition-dependent electrocatalytic properties of the AuAg nanocages are investigated in depth for catalysis of MOR. The obtained hollow AuAg cubic nanocages exhibit excellent catalytic properties for MOR because of their optimized composition, unique porous walls, and hollow nanostructure. These properties increase the specific surface area and active catalytic sites. Doping with Ag enhances the catalytic activity and prevents the CO poisoning of the Au catalyst. The functions of Ag doping in the catalytic performance of the AuAg nanocage are also studied using density functional theory (DFT) calculation method.

2. Results and Discussion

Hollow Au and AuAg nanocages were synthesized via a galvanic reaction using Cu_2O nanoparticles as the templates. The proposed formation mechanism and process of the hollow nanocages in this synthesis system are illustrated in a schematic diagram in **Figure 1**a. Accordingly, the growth process of the Au cubic nanocage was recorded using the transmission electron microscopy (TEM) images which were obtained with the sample being synthesized at different times (Figure S1, Supporting Information). Cubic Cu_2O nanoparticles were used as the sacrificial template in the synthesis of Au cubic nanocages. First, the galvanic reaction occurred on the surface of Cu_2O nanoparticles. The electrons were transferred from the monovalent Cu^+ ions in Cu_2O to Au^{3+} ions, and thus, Cu^+ changed to Cu^{2+}; Au^{3+} was reduced to Au atoms during the galvanic reaction. Correspondingly, the produced Cu^{2+} dissolved in the solution, and the reduced Au atoms were deposited on the surface of the Cu_2O nanoparticles (Figure S1a, Supporting Information). A heterojunction formed between Au and Cu_2O, and this drove the transfer of electrons to the Au metal on the surface. Thus, Au^{3+} ions were reduced and deposited on the surface of cubic Cu_2O, and the center part of the Cu_2O nanoparticles was etched into hollow structures (Figure S1b,c, Supporting Information). Finally, Au nanoparticles contacted each other to form porous wall of nanocages through the Ostwald ripening process (Figure S1d,e, Supporting Information). Figure 1b shows the scanning electron microscopy (SEM) image of the Cu_2O nanocubes that are used as the sacrificial template to synthesize the Au cubic nanocages. The Cu_2O nanocubes are uniform in both morphology and size. As shown in the inset image of Figure 1b, the average side length of the nanocube is ≈180 nm. Figure 1c shows the SEM image of the Au cubic nanocages synthesized using the Cu_2O nanocubes as a sacrificial-template. The Au cubic nanocages are consistent with the

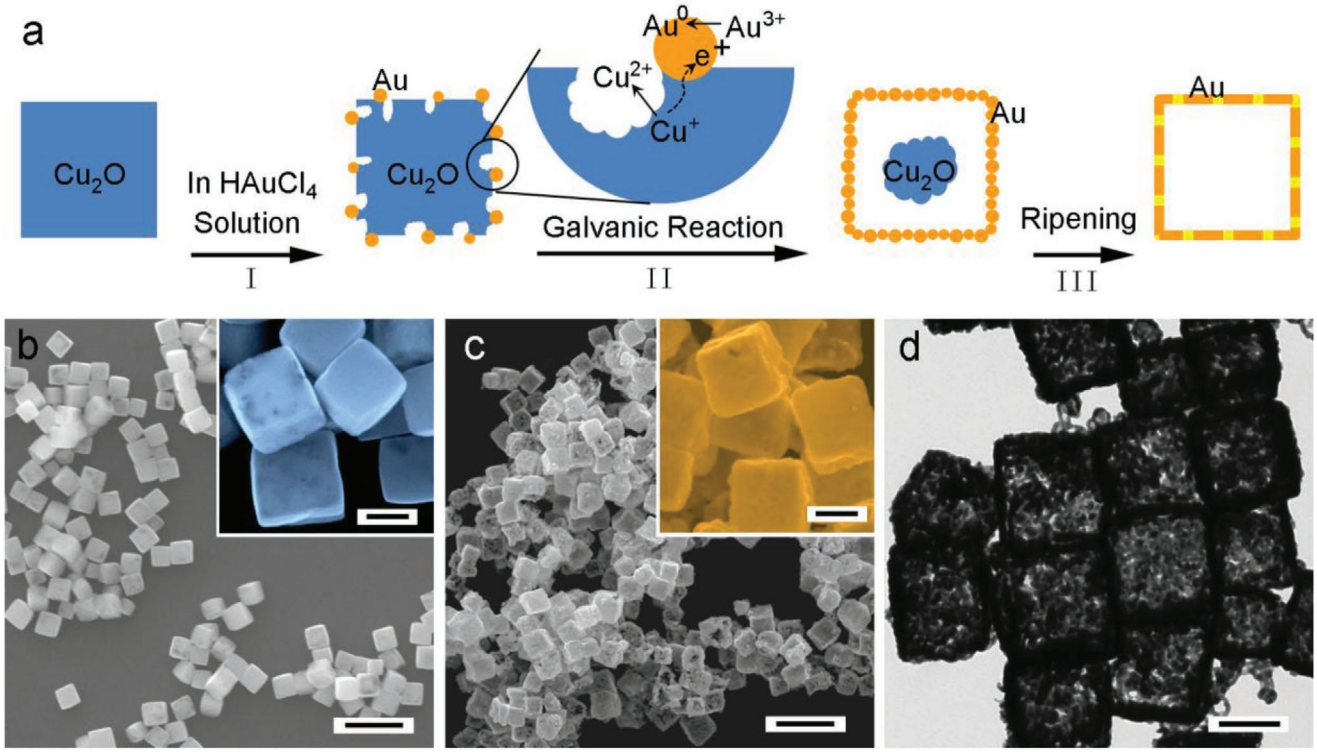

Figure 1. a) Schematic diagram for the formation process of Au nanocages using Cu_2O nanocubes as a sacrificial template. SEM images of b) Cu_2O nanocubes and c) Au cubic nanocages (scale bars are 500 nm). The insets in (b) and (c) are magnified SEM images (scale bars are 100 nm). d) TEM image of Au cubic nanocages (scale bars are 100 nm).

Cu_2O templates in terms of size and shape. The average side length of the Au cubic nanocages is also nearly 180 nm (inset of Figure 1c). The surface of the obtained Au cubic nanocage is rough that is different with the smooth surface of Cu_2O templates. As seen in the TEM image in Figure 1d, the rough surface of the Au cubic nanocage is constructed with a porous nanostructure. The result of TEM and SEM images indicates that the Au cubic nanocages have a hollow center and a porous wall. The elemental composition of the Au cubic nanocages was analyzed using energy-dispersive X-ray spectroscopy (EDX) and inductively coupled plasma atomic emission spectroscopy (ICP-AES). The results from these analyses show that there is only Au metal in the Au nanocages, and the Si signal (Figure S2, Supporting Information) in the EDX data comes from the substrate.

In addition to the cubic Au nanocages, octahedral Au nanocages were also successfully synthesized via the galvanic reaction using the octahedral Cu_2O nanoparticles as the sacrificial templates. Figure S3 in the Supporting Information shows the SEM image of the octahedral Cu_2O templates. Figures S4 and S5 in the Supporting Information show the SEM and TEM images of the obtained Au octahedral nanocages, respectively. Similar to the cubic nanocages, the octahedral nanocages also possess a hollow center and a porous wall. The EDX analysis (Figure S6, Supporting Information) also indicates that there is only Au metal in the octahedral nanocages.

In synthesizing the Au nanocages, when the Ag precursor was further added, AuAg alloy nanocages were obtained. **Figure 2**a,c is the TEM image and high-angle annular dark-field scanning transmission electron microscopy (HAADF-STEM) image of cubic AuAg alloy nanocages, respectively. The AuAg alloy nanocages have the same morphology and nanostructure as the pure Au nanocages and the thickness of the porous wall is ≈20 nm. The selected-area electron diffraction (SAED) pattern (inset in Figure 2a) indicates that the porous wall of the AuAg alloy nanocages is polycrystalline. Figure 2b presents the high-resolution (HR)-TEM image, which shows that the porous wall of the nanocage is formed through the sintering of AuAg nanoparticles. The crystalline directions (indicated by arrows in Figure 2b) of each nanoparticle are different. The cold sintering between these nanoparticles induced a grain boundary and a terrace on the surface. EDX analysis (Figure S7, Supporting Information) proves that the Ag precursor is reduced and that Ag metal is present in the nanocage. Figure 2d,e shows EDX composition maps of Au and Ag in the hollow cubic nanocage, respectively, within the region indicated by the circle in Figure 2c. The same distribution of the Au and Ag compositions in the map shows that the Au and Ag atoms are highly intermixed. Figure 2f,g, respectively, shows the results of EDX elemental linear scans along lines A and B (indicated in Figure 2c), and these scans indicate the homogenous alloy nature of the AuAg nanocages.

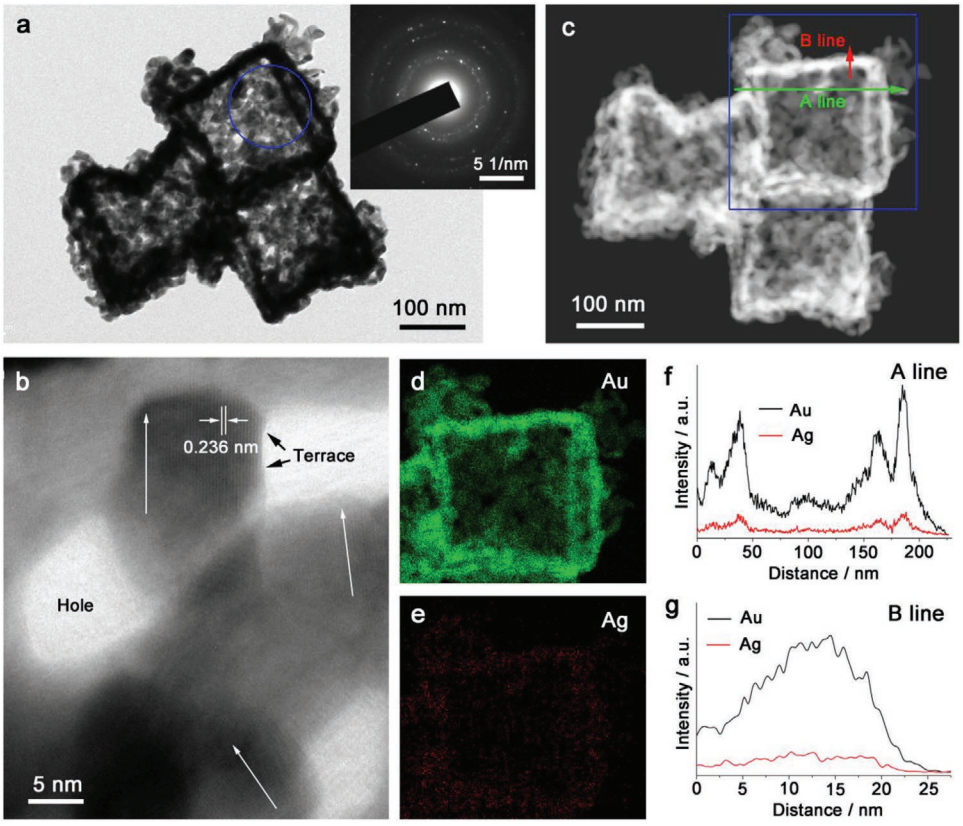

Figure 2. a) TEM image of the AuAg cubic nanocages and the corresponding SAED patterns obtained from the circled area. b) HR-TEM image of the AuAg cubic nanocages. c) Representative HAADF-STEM image in combination with d,e) EDX elemental maps for the area indicated by the square and f,g) EDX elemental linear scans along the A line and B lines.

The amount of Ag metal in the AuAg cubic nanocages was determined using ICP-AES, and the result shows that there is 5 at% Ag metal in the sample. **Figure 3** shows the X-ray photoelectron spectroscopy (XPS) spectra of the Au and AuAg cubic nanocages. The XPS peaks for the Au cubic nanocage can be attributed to the Au element and matches well with the standard binding energies of pure Au (Au 4f7/2, 84.0 eV; Au 4f5/2, 87.7 eV) (Figure 3a and Figure S8, Supporting Information). For the XPS of AuAg cubic nanocages, the two peaks of Au 4f (Figure 3c) are shifted to higher energies a little with values of 84.08 and 87.79 eV, respectively, compared with the pure Au materials. The two peaks of Ag 4d (Figure 3d) are shifted to lower energies with values of 367.9 and 374.0 eV, respectively, compared with the standard binding energies of pure Ag metals (368.2 and 374.2 eV). These shifts in binding energies suggest that the electron transfer from Au to Ag in the bimetallic AuAg nanocages is related to the formation of the AuAg alloy. The ratio of Ag atoms in the alloy is much lower than that of Au atoms, thus the more shift of Ag 4d peaks than that of Au 4f indicates that Ag atoms are well dispersed in the alloy materials.[34] Figure S9 in the Supporting Information shows the powder X-ray diffraction (PXRD) patterns of the cubic Cu_2O templates and the obtained cubic AuAg nanocages. The five diffraction peaks in the PXRD patterns are consistent with those of the AuAg alloy metal with an FCC (face-centered cubic) structure that corresponds to the (111), (200), (220), (311), and (222) planes. After synthesis, the signals of the residual Cu_2O templates can be clearly removed. The composition ratio of Ag metal in the AuAg nanocage can be changed by adjusting the feed ratio of the Ag precursor.

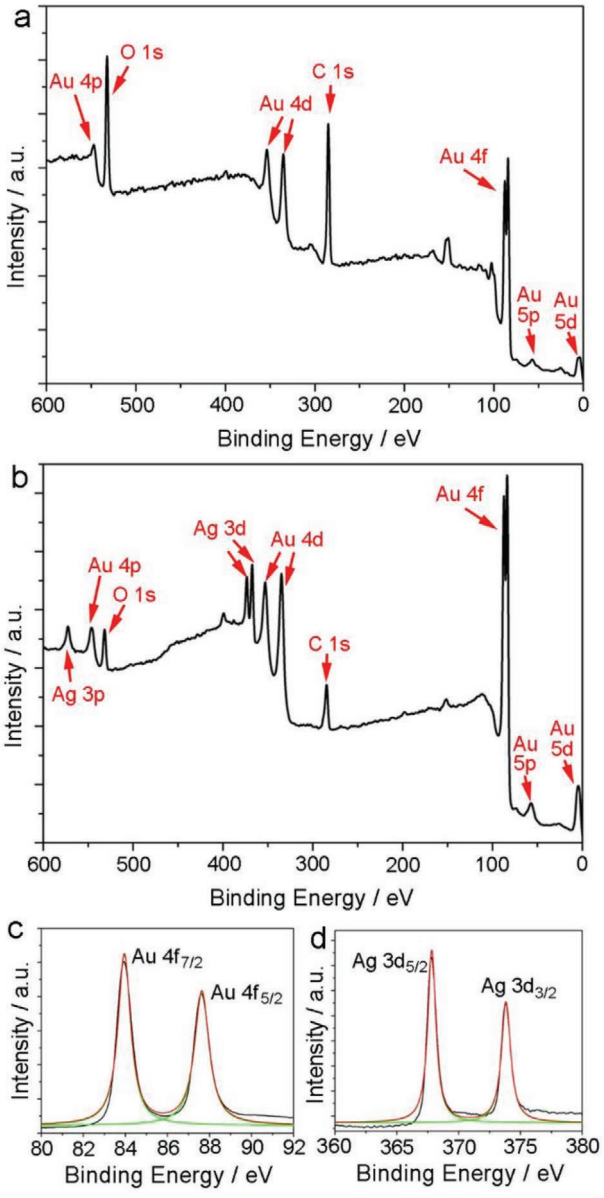

Figure 3. XPS spectra of a) the Au cubic nanocages and b) the AuAg cubic nanocages. c) Au 4f and d) Ag 3d XPS spectra for the AuAg cubic nanocages.

The Au and AuAg nanocages have hollow structures and porous walls, and these characteristics lead to a large surface area-to-volume ratio and a high specific catalytic area. On the other hand, there are plenty of crystalline dislocations in the grain boundary and a high density of low-coordinated atoms at the surface terrace twin planes. These are active sites in the electrocatalytic reaction. Therefore, the as-prepared Au and AuAg nanocages are potentially ideal electrocatalytic candidates that will have enhanced catalytic activity. We perform electrocatalysis of the MOR as a model reaction for investigating the catalytic activity of the obtained Au and AuAg nanocages. First, the catalytic property of pure Au metal nanocages with different morphologies, including Au cubic nanocages and Au octahedral nanocages, was evaluated and compared with the spherical Au nanoparticles. The size of Au nanoparticles is around 25 nm, and this is similar to the size of the connected nanoparticles in the porous walls of the Au or AuAg nanocages. **Figure 4**a presents the cyclic voltammetry (CV) curves of MOR with the three catalysts (Au cubic nanocages: Au CNCs, Au octahedral nanocages: Au ONCs, and Au nanoparticles: Au NPs). The CV measurement was performed in an argon gas-purged 0.5 M KOH and 2 M CH_3OH solution using a glassy carbon rotating disk electrode as the working electrode at room temperature with a scan rate of 50 mV s^{-1}. The CV curves demonstrate little difference in the shape among these three catalysts, suggesting a similar reaction pathway and exhibiting the characteristic methanol electrooxidation behavior.[39] The instant surge in current was started from −0.10 V (vs Ag/AgCl) onward in the positive potential scan. The peaks between 0.2 and 0.3 V (depending on different catalysts) correspond to the oxidation peak of methanol.[40,41]

In the reverse sweeping scan, a reduction current peak was observed at around 0.12 V, indicating the reduction of Au-OH to Au.[42] A second current peak in the reverse scan was located at around 0.0 V, which is attributed to the removal of the incompletely oxidized carbonaceous species, such as carbon monoxide. Compared with solid Au nanoparticles, the hollow and porous Au nanocages exhibit higher catalytic activity for MOR. Our hollow Au cubic nanocages and hollow Au octahedral nanocages have peak currents that are 4.1 times and 2.8 times higher than the peak current of the Au nanoparticles.

Electrochemical oxide stripping reaction of Au in 0.5 M sulfuric acid aqueous solution at a scan rate of 10 mV s^{-1} in room

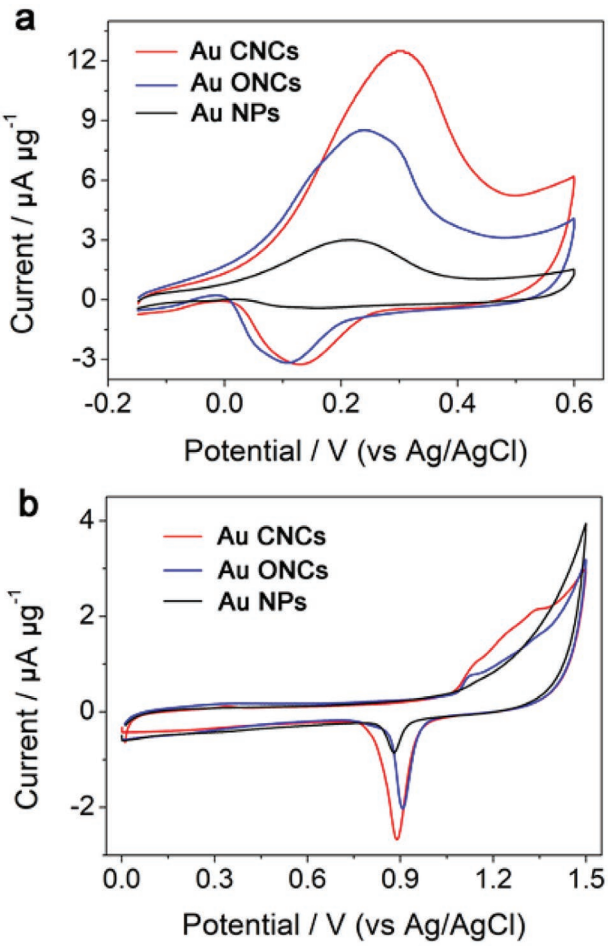

Figure 4. a) Cyclic voltammograms (CVs) of electro-methanol oxidation, and b) oxide stripping curves of the Au cubic nanocages (Au CNCs), Au octahedral nanocages (Au ONC), and Au nanoparticles (Au NPs).

temperature was carried out to estimate the electrochemical active surface area of the Au cubic nanocages, Au octahedral nanocages, and Au nanoparticles (Figure 4b). The oxidation potential of the hollow and porous Au nanocages is lower (starting at around 1.1 V) than that of solid Au nanoparticles, indicating that the low-coordinated atoms on the surface of the Au nanocages are more easily oxidized. The area of current curve that peaks near 0.9 V due to the gold oxide reduction can be integrated to estimate the electrochemically active surface areas (ECSAs), assuming a specific charge of 450 μC cm^{-2} for the gold oxide reduction.[34] The ECSAs of the Au cubic nanocages, Au octahedral nanocages, and Au nanoparticles are 5.65, 3.98, and 1.35 m^2 g^{-1}, respectively. Although, the size of the Au nanoparticles resembles the connected nanoparticles in the porous walls of the nanocages, the electrochemical active surface area is much lower than that of the nanocages. Aggregation and welding of Au nanoparticles on the electrode during the electrochemical measurement induces a decrease in the active surface area. The enhanced catalytic performance of the Au nanocages can be attributed to the high density of low coordinated atoms present at the terrace and island in the porous walls of the nanocages that have high chemical activity.

Furthermore, the hollow and highly porous nanostructure and large specific electrochemical active surface area facilitate the mass transfer and diffusion of electrolyte to the catalytically active surface for reaction.

In addition to studying the morphology and nanostructure, we studied the effects of composition of Ag doping on the electrocatalytic properties of the Au nanocages for MOR. In a previous report, Fujita and co-workers found that adding a small amount of Ag to Au nanocrystals significantly improves the catalytic activity for the oxidation of carbon monoxide.[43] Because the cubic nanocages possess higher catalytic active than octahedral nanocage, we synthesized AuAg cubic nanocages with different ratios of Ag to Au. The morphology, crystal structure, and composition distribution of the typical AuAg cubic nanocage with 5 at% Ag were studied in depth, characterized, and discussed (Figures 2 and 3 and Figures S7 and S9, Supporting Information). The electrocatalytic activities of the AuAg nanocages for MOR with different atomic ratio of Ag were measured, and the result are shown in **Figure 5**. Compared with the Au nanocages (0% Ag), the CV curves of AuAg alloy nanocages for MOR in 0.5 M KOH and 2 M CH_3OH aqueous solution with a scan rate of 50 mV s^{-1} are similar, and this result indicates the same catalytic reaction pathway for Au and AuAg nanocages. The addition of Ag atoms in the AuAg alloy nanocages greatly improves the catalytic property for the methanol electrooxidation. The AuAg cubic nanocage with 5 at% Ag has a maximum methanol oxidation peak current of 22.1 μA $μg^{-1}$. This peak current is 1.8 times greater than that of the Au cubic nanocage (0 at% Ag) and 7.4 times greater than that of Au nanoparticle. When the Ag composition is increased to 10 at%, the peak current of the AuAg alloy cubic nanocages decreases to 19.7 μA $μg^{-1}$, and this result indicates that only a small amount of added Ag may improve the catalytic activity. The promotional function of doping Ag in the electrocatalytic MOR also has been reported in published papers.[24,34,45,46] For the mass activity, our AuAg cubic nanocages show enhanced property than reported hollow AuAg nanourchins and mesoporous AuAg nanoparticles,[24,34] and less than reported hollow mesoporous AuAg nanospheres.[45,46] Compared with hollow mesoporous AuAg nanospheres, our AuAg cubic nanocages possess less ECSA

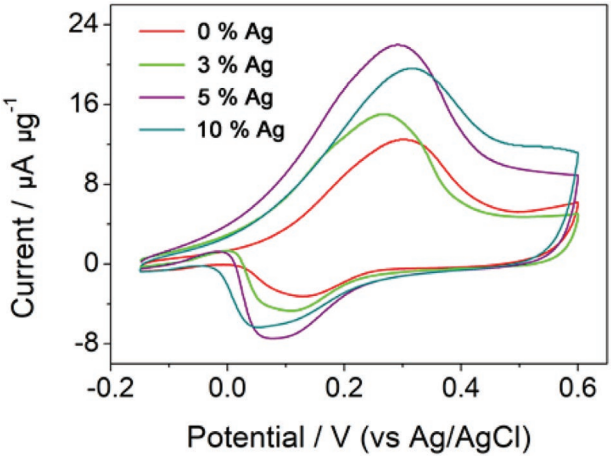

Figure 5. Cyclic voltammograms (CVs) of electro-methanol oxidation of the AuAg cubic nanocages with Ag atomic ratios of 0%, 3%, 5%, and 10%.

due to the larger thickness of the porous wall than hollow mesoporous AuAg nanospheres, which will induce the less mass activity. However, compared from specific activity, our AuAg cubic nanocages show enhanced catalytic activity than previously reported AuAg nanourchins and mesoporous AuAg nanoparticles.[24,34,45,46] The distinctly improved specific activity may be owing to the clean surface of AuAg cubic nanocages that without surfactants are used in the synthesis.[39,47]

We used DFT to further study the mechanism of Ag doping in the improvement of the electrocatalytic properties. Previous reports show that the d-band electrons of noble metal nanocatalysts play the dominant role in the electrocatalytic reaction process. The density of states (DOS) and d-band center are usually calculated to evaluate and analyze catalytic properties of noble metal nanocrystals.[48,49] We built four kinds of $4 \times 4 \times 4$ periodic crystal cells with different ratios of Au and Ag atoms and optimized the FCC cell using DFT. Figure S10 in the Supporting Information shows the d-band DOS curves of $Au_{64}Ag_0$, $Au_{62}Ag_2$, $Au_{60}Ag_4$, and $Au_{56}Ag_8$ as calculated from the bulk and the (100) surface using DFT methods. These curves are very similar in morphology, and this result indicates that doping with a small amount of Ag has no obvious effect on the DOS of Au metal crystal. The d-band center also was calculated, and the results are summarized in **Table 1**. With an increase in Ag content, the d-band center moves to low energy, but the movement is not significant. Compared with $Au_{64}Ag_0$, the d-band center of $Au_{56}Ag_8$ moves only 0.026 and 0.046 eV for the bulk and the (100) surface, respectively.

The adsorption of reactant molecules on the surface of nanocatalysts is considered to be one of the key factors that significantly influence heterogenous catalysis reactions.[50,51] The adsorption energy of methanol molecules on the AuAg alloy surface was calculated using DFT method. **Figure 6**a,c shows the typical optimized configurations of one methanol molecule adsorbed on the (100) and (111) surfaces of AuAg alloy. In a practical oxidation catalytic process, the atoms near the surface of the alloy nanocrystal may be redistributed. The Somorjai research group reported that relatively active metal atoms in noble metal alloy nanoparticles would diffuse to the surface under oxidizing conditions.[52] In the catalytic reaction system for MOR, the methanol has stronger adsorption with Ag atoms on the AuAg nanocatalysts, and thus the Ag atoms near the surface will diffuse to the surface. Figure 6b,d shows the adsorption energies of methanol on the surface of the AuAg alloy crystal with different numbers of Ag atoms on the surface. The names of Au, AuAg1, AuAg2, AuAg3, and AuAg6 are noted for the AuAg crystals with 0, 1, 2, 3, and 6 Ag atoms, respectively, on the periodic 4×4 surface. The DFT results indicate that the adsorption intensity of methanol molecules on the AuAg surface is highly related to the ratio of Ag atoms. For both the (100) and (111) surfaces, the adsorption energy increases with an increase in the number of Ag atoms on the surface from 0 to 3, and then it decreases with a further increase in the number of Ag atoms. The adsorption energy reaches a maximum on both the (100) and (111) surfaces when there are 3 Ag atoms on the periodic 4×4 AuAg surface.

Table 1. Values of the d-band center obtained from DFT for the Au and AuAg alloy crystals. (Unit: eV).

	Bulk	(100) Surface
Au	−3.685	−3.297
$Au_{97}Ag_3$	−3.691	−3.305
$Au_{94}Ag_6$	−3.702	−3.332
$Au_{88}Ag_{12}$	−3.711	−3.343

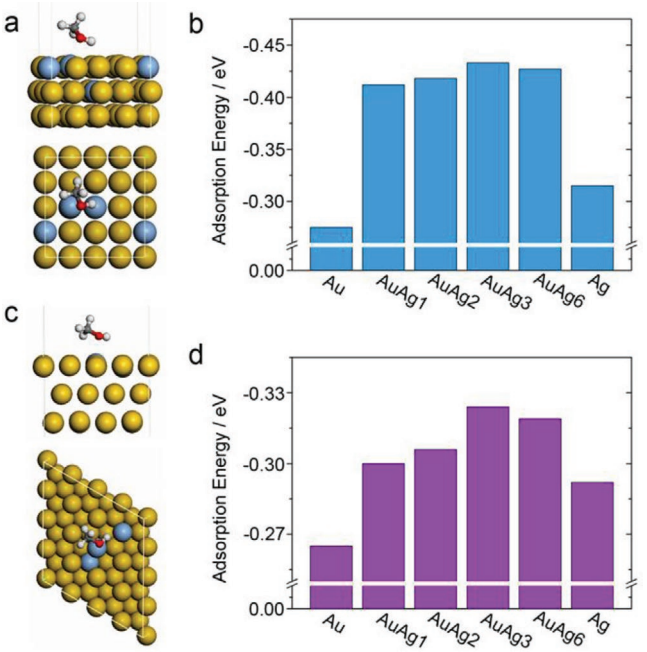

Figure 6. Optimized configurations of a methanol molecule adsorbed on the a) AuAg3 (100) and c) AuAg3 (111) surfaces in a periodic cell, calculated using DFT method. Adsorption energies of methanol molecule on Au, Ag, and AuAg alloy at the b) (100) and d) (111) surfaces.

The adsorption of methanol on the AuAg alloy surface may explain the function of Ag in the improved catalytic reaction. A small amount of Ag atoms doped in the AuAg alloy promotes the adsorption of methanol on the catalyst surface and then accelerates the catalytic reaction. When there are too many Ag atoms added to the AuAg alloy, the adsorption of methanol is weaker, and the catalytic reaction slows. Besides the adsorption energy of methanol molecule, the deprotonation process of methanol molecule on the Au and AuAg alloy surfaces was also calculated following the previous report.[51] **Figure 7**a shows the typical DFT-optimized configurations of methanol molecule during the deprotonation process on the AuAg alloy (100) surface. As shown in Figure 7b, the activation barriers for the deprotonation of methanol molecule display a volcanic vent shape along the increase of the doping amount of Ag. The doping with a small amount of Ag would obviously decrease the active barrier for the deprotonation of methanol on the AuAg alloy surface. However, the excess adding of Ag would increase the active barrier. This theory result is consistent with our experimental result, as shown in Figure 5, that only doping with small amount (about 5%) of Ag would promote the electrocatalytic activities of AuAg alloy for the MOR.

The other factor for the catalytic properties is the desorption of carbon monoxide (CO), which always induces the poisoning

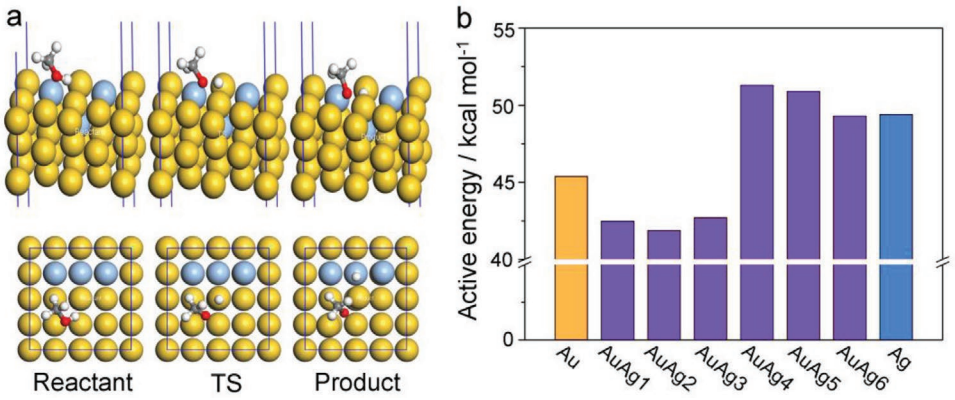

Figure 7. a) Configurations of the reactant (R), transition state (TS), and product (P) for the deprotonation of methanol on the AuAg3 (100) surfaces in a periodic cell, calculated using DFT method. b) Energy barrier for the deprotonation of methanol on the Au, AuAg, and Ag (100) surface.

of metal nanocatalysts. We also calculated the adsorption energies of CO molecule on the Au, AuAg, and Ag (100) surface using DFT method. As shown in Figure S11 in the Supporting Information, the doping of Ag displays no obvious effect on the adsorption energy of CO on AuAg alloy surface, compared with that on pure Au and Ag surface. Thus, the mechanism of the enhancement catalytic properties of AuAg alloy can be attributed to the increase of adsorption energy of methanol and decrease of active energy for the deprotonation of methanol on the AuAg alloy surface.

To evaluate the tolerance and long-term electrocatalytic performance of hollow AuAg nanocages in MOR, we study the chromoamperograms of the AuAg CNCs with 5 at% Ag and compare the results with those of Au NPs and pure Au CNCs. The current–time response of each of the three catalysts was recorded at their respective oxidative peak potentials, and the results are shown in **Figure 8**. During the 2000 s chronoamperometry process, the polarization currents for each of the three catalysts decreased rapidly during the early stage, because of the formation of intermediate species during MOR. In comparison, the current of the AuAg cubic nanocages exhibits a gradual and slower decrease over the whole stage. The decreasing rate of the current lagged, and this indicates that the electrocatalytic stability of the AuAg cubic nanocages is higher than that of the Au nanoparticles and Au cubic nanocages. The TEM images of AuAg hollow nanocages before and after the 2000 s chronoamperometry process are shown in Figure S12 in the Supporting Information. After the chronoamperometry test, the morphology of AuAg nanocages have no obviously change, indicating that the hollow structure possesses enhanced stability during the electrocatalysis process.

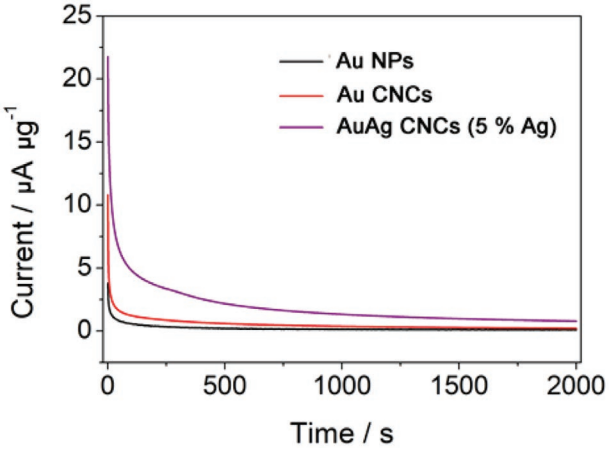

Figure 8. Chronoamperograms of Au nanoparticles (NPs), Au cubic nanocages (CNCs), and AuAg cubic nanocages (CNCs) in a deoxygenated solution of 0.5 M KOH and 2 M CH_3OH.

3. Conclusion

In summary, well-designed Au and AuAg alloy hollow nanocages were controllably synthesized by using Cu_2O nanoparticles as sacrificial templates. As free-standing catalysis, the AuAg cubic nanocages have greatly enhanced electrocatalytic properties for MOR because they have the following advantages: 1) The hollow and porous nanostructure supports a large electrochemically active surface area. 2) The large surface area-to-volume ratio of nanocages facilitates the diffusion and mass transfer of electrolyte to the catalytically active surface for reaction. 3) There are many low-coordinated atoms present at the terrace and in the island on the surface, and these serve as highly active electrocatalytic points. 4) The nanocages were synthesized without using any capping agents, and thus the surface is very clean for electrocatalysis. 5) Doping with optimal amount of Ag further greatly improves the catalytic activity for MOR. In addition, the mechanism of Ag doping in the promotional function to the catalytic properties was investigated in depth using DFT. The DFT result indicates that a small amount of Ag atoms doped in the AuAg alloy may promote the adsorption of methanol and decrease the active energy for the deprotonation of methanol on the AuAg alloy surface. With the combination of these advantages, we expect our hollow and porous AuAg nanocages to have an important impact on the development of fuel cell catalysts, including both of scalable synthesis and high catalytic performance.

4. Experimental Section

Materials: Cupric chloride ($CuCl_2{\cdot}2H_2O$) 99.99%, sodium hydroxide (NaOH) ≥98%, silver nitrate ($AgNO_3$) ≥90%, ascorbic acid ($C_6H_8O_6$)

≥99%, gold (III) chloride hydrate ($HAuCl_4{\cdot}4H_2O$) 99.999%, hydrazine monohydrate ($N_2H_4{\cdot}H_2O$) >98%, and ammonia solution ($NH_3{\cdot}H_2O$) ≥25% were purchased from Aladdin. All aqueous solutions were prepared using deionized (DI) water that had a resistivity of 18.2 MΩ cm.

Synthesis of Cu_2O Nanoparticles: The synthesis of Cu_2O nanoparticles was performed following the procedure that previously reported by Wang group.[38] For the synthesis of cubic Cu_2O nanoparticles, 1 mL of $CuCl_2$ solution (0.1 M) and 1 mL of NaOH solution (0.2 M) were added to 50 mL of DI water under constant stirring for 5 min. Then, 1 mL of ascorbic acid solution (0.1 M) was added. The color of the precipitates turned from blue to yellow and then to brick-red in 1 min. Finally, centrifugation (4000 rpm, 1 min) was used to quickly separate the precipitates. The precipitates were washed several times with DI water and ethanol. The method for the synthesis of octahedral Cu_2O nanoparticles was similar to that used for the synthesis of cubic nanoparticles, except that the concentration of the NaOH solution was 0.3 M and 2 mL of hydrazine hydrate solution (1 M) was used instead of the ascorbic acid solution. After adding hydrazine hydrate, the reaction time was prolonged to 20 min.

Synthesis of Au and AuAg Nanocages: In a typical synthesis of AuAg nanocages, a certain amount of Cu_2O suspension was dispersed into 30 mL of DI water under constant stirring for 5 min. While being stirred, a certain amount of $AgNO_3$ (30×10^{-3} M) was injected into the solution. After 5 min of stirring, a certain amount of $HAuCl_4$ (10×10^{-3} M) was added with continue stirring for 10 min. Centrifugation (4000 rpm, 1 min) was used to separate the products, which were dispersed in ammonia solution (18%) for 10 h to remove the remaining Cu_2O template. Centrifugation was then used to separate the products, which were dispersed in HNO_3 solution (1%) to remove the unalloyed Ag metal. Finally, the product was washed with DI water several times. The synthesis of Au nanocages was similar to that of AuAg nanocages, except $AgNO_3$ was not added.

Characterization: SEM images were recorded using a JSM-7000F field-emission scanning electron microscope at an accelerating voltage of 10 kV. TEM and HR-TEM images were recorded using a JEM-2100 microscope at an accelerating voltage of 200 kV. An HAADF-STEM image, EDX elemental line-scanning, and EDX elemental mapping were recorded using a TEM-2100F microscope at an accelerating voltage of 200 kV. XPS measurements were made using an AXIS ULtrabld X-ray photoelectron spectrometer. XRD patterns were obtained using a BRUKER D8 ADVANCE X-ray diffractometer with a Cu KR X-ray source ($\lambda = 1.5405$ Å).

Electrochemical Measurements: The electrochemical reaction was measured using a VersaSTAT3 electrochemical work station and was performed in a three-electrode electrochemical cell. The working electrode was a glassy carbon electrode with a 5 mm diameter. A quantity of 1 mg of Au or AuAg nanocage sample was dispersed in 1 mL ethanol using ultrasonication. A quantity of 20 µL of this solution was drop-cast on the surface of the glassy carbon electrode. The electrode was air dried at room temperature. After evaporating the water, 10 µL of Nafion solution (0.05 wt%, diluted from 5 wt% Nafion, Ion Power, Inc.) was covered on the surface and dried under atmospheric conditions. A 1 cm^2 platinum foil was used as the counter electrode, and a saturated Ag/AgCl electrode was used as the reference electrode. The MOR was performed in 0.5 M KOH and 2 M CH_3OH solution using CV at a scan rate of 50 mV s^{-1} at room temperature. The CV in 0.5 M H_2SO_4 aqueous solution at a scan rate of 10 mV s^{-1} at room temperature was used to estimate the electrochemical active surface area.

Supporting Information

Supporting Information is available from the Wiley Online Library or from the author.

Acknowledgements

This work was supported by the programs supported by the National Natural Science Foundation of China (nos. 21675122, 21874104, 22074115), the Key Research Program in Shaanxi (2017NY-114), Zhejiang Provincial Natural Science Foundation of China (no. LY20E010007), and Natural Science Foundation of Shaanxi Province (no. 2019JLP-19), the World-Class Universities (Disciplines) and the Characteristic Development Guidance Funds for the Central Universities.

Conflict of Interest

The authors declare no conflict of interest.

Data Availability Statement

The data that support the findings of this study are available from the corresponding author upon reasonable request.

Keywords

AuAg alloys, electrocatalysts, hollow and porous nanostructures, methanol oxidation reaction (MOR)

Received: November 8, 2021
Revised: November 15, 2021
Published online:

[1] H. J. You, S. C. Yang, B. J. Ding, H. Yang, *Chem. Soc. Rev.* **2013**, *42*, 2880.
[2] J. Zhu, L. S. Hu, P. X. Zhao, L. Y. S. Lee, K. Y. Wong, *Chem. Rev.* **2020**, *120*, 851.
[3] Y. T. Pan, H. Yang, *Nano Today* **2020**, *31*, 100832.
[4] Y. N. Xia, X. H. Xia, H. C. Peng, *J. Am. Chem. Soc.* **2015**, *137*, 7947.
[5] X. J. Wang, J. Feng, Y. C. Bai, Q. Zhang, Y. D. Yin, *Chem. Rev.* **2016**, *116*, 10983.
[6] M. K. Debe, *Nature* **2012**, *486*, 43.
[7] Y. Jiao, Y. Zheng, M. T. Jaroniec, S. Z. Qiao, *Chem. Soc. Rev.* **2015**, *44*, 2060.
[8] W. Zhu, Z. Chen, Y. Pan, R. Y. Dai, Y. Wu, Z. B. Zhuang, D. S. Wang, Q. Peng, C. Chen, Y. D. Li, *Adv. Mater.* **2019**, *31*, 1800426.
[9] H. J. You, J. X. Fang, *Nano Today* **2016**, *11*, 145.
[10] V. R. Stamenkovic, D. Strmcnik, P. P. Lopes, N. M. Markovic, *Nat. Mater.* **2017**, *16*, 57.
[11] K. D. Gilroy, A. Ruditskiy, H. C. Peng, D. Qin, Y. N. Xia, *Chem. Rev.* **2016**, *116*, 10414.
[12] J. Jones, H. F. Xiong, A. T. Delariva, E. J. Peterson, H. Pham, S. R. Challa, G. S. Qi, S. Oh, M. H. Wiebenga, X. I. P. Hernandez, Y. Wang, A. K. Datye, *Science* **2016**, *353*, 150.
[13] H. Lv, A. Lopes, D. D. Xu, B. Liu, *ACS Cent. Sci.* **2018**, *4*, 1412.
[14] H. J. You, F. L. Zhang, Z. Liu, J. X. Fang, *ACS Catal.* **2014**, *4*, 2829.
[15] Z. B. Yang, L. Zhang, H. J. You, Z. Y. Li, J. X. Fang, *Part. Part. Syst. Charact.* **2014**, *31*, 390.
[16] T. Radhakrishnan, N. Sandhyarani, *Electrochim. Acta* **2019**, *298*, 835.
[17] J. B. Ding, L. Z. Bu, S. J. Guo, Z. P. Zhao, E. B. Zhu, Y. Huang, X. Q. Huang, *Nano Lett.* **2016**, *16*, 2762.
[18] M. Tang, S. P. Luo, K. Wang, H. Y. Du, R. Sriphathoorat, P. K. Shen, *Nano Res.* **2018**, *11*, 4786.
[19] T. Kwon, M. Jun, H. Y. Kim, A. Oh, J. Park, H. Baik, S. H. Joo, K. Lee, *Adv. Funct. Mater.* **2018**, *28*, 1706440.
[20] A. Mahmood, N. H. Xie, M. A. U. Din, F. Saleem, H. F. Lin, X. Wang, *Chem. Sci.* **2017**, *8*, 4292.
[21] H. Y. Kim, J. M. Kim, Y. Ha, J. Woo, A. Byun, T. J. Shin, K. H. Park, H. Y. Jeong, H. Kim, J. Y. Kim, S. H. Joo, *ACS Catal.* **2019**, *9*, 11242.

[22] R. Boukil, N. Tuleushova, D. Cot, B. Rebiere, V. Bonniol, J. Cambedouzou, S. Tingry, D. Cornu, Y. Holade, *J. Mater. Chem. A* **2020**, *8*, 8848.
[23] T. Li, H. J. You, M. W. Xu, X. P. Song, J. X. Fang, *ACS Appl. Mater. Interfaces* **2012**, *4*, 6942.
[24] L. Yu, L. Zhang, X. Zhang, G. Dai, J. Zhang, X. Wang, H. You, *ACS Appl. Energy Mater.* **2019**, *3*, 723.
[25] S. J. Guo, S. Zhang, X. L. Sun, S. H. Sun, *J. Am. Chem. Soc.* **2011**, *133*, 15354.
[26] H. J. Huang, S. B. Yang, R. Vajtai, X. Wang, P. M. Ajayan, *Adv. Mater.* **2014**, *26*, 5160.
[27] H. J. You, Y. Y. Xuan, Y. Zuo, F. Shen, X. G. Han, J. X. Fang, *Nanotechnology* **2018**, *29*, 425708.
[28] J. Jones, H. Xiong, A. T. DeLaRiva, E. J. Peterson, P. Hien, S. R. Challa, G. Qi, S. Oh, M. H. Wiebenga, X. I. P. Hernandez, Y. Wang, A. K. Datye, *Science* **2016**, *353*, 150.
[29] Z. Mao, H. H. Hu, R. Su, P. Z. Liu, Y. X. Li, W. T. Zhang, X. N. Zhao, J. J. Guo, P. F. Guan, G. W. Qin, X. F. Zhang, *ChemCatChem* **2018**, *10*, 141.
[30] J. X. Fang, J. Li, C. F. Tian, Q. Q. Gao, X. J. Wang, N. Y. Gao, X. L. Wen, C. S. Ma, H. J. You, Z. L. Yang, Q. H. Xu, Q. H. Xiong, Z. Y. Li, *NPG Asia Mater.* **2016**, *8*, e323.
[31] M. U. Khan, H. J. You, X. T. Liu, L. L. Zhang, J. X. Fang, *Small* **2018**, *14*, 1702948.
[32] W. Li, J. Liu, D. Y. Zhao, *Nat. Rev. Mater.* **2016**, *1*, 16023.
[33] H. J. Wang, H. Y. Jeong, M. Imura, L. Wang, L. Radhakrishnan, N. Fujita, T. Castle, O. Terasaki, Y. Yamauchi, *J. Am. Chem. Soc.* **2011**, *133*, 14526.
[34] J. X. Fang, L. L. Zhang, J. Li, L. Lu, C. S. Ma, S. D. Cheng, Z. Y. Li, Q. H. Xiong, H. J. You, *Nat. Commun.* **2018**, *9*, 521.
[35] S. H. Han, H. M. Liu, P. Chen, J. X. Jiang, Y. Chen, *Adv. Energy Mater.* **2018**, *8*, 1801326.
[36] Z. M. Peng, H. J. You, J. B. Wu, H. Yang, *Nano Lett.* **2010**, *10*, 1492.
[37] L. Zhang, L. T. Roling, X. Wang, M. Vara, M. F. Chi, J. Y. Liu, S. I. Choi, J. Park, J. A. Herron, Z. X. Xie, M. Mavrikakis, Y. N. Xia, *Science* **2015**, *349*, 412.
[38] Z. H. Wang, H. Wang, L. L. Wang, L. Pan, *Cryst. Res. Technol.* **2009**, *44*, 624.
[39] H. J. You, W. J. Wang, S. C. Yang, *ACS Appl. Mater. Interfaces* **2014**, *6*, 19035.
[40] X. X. Yan, S. J. Yu, Y. W. Tang, D. M. Sun, L. Xu, C. Xue, *Nanoscale* **2018**, *10*, 2231.
[41] S. Pedireddy, H. K. Lee, C. S. L. Koh, J. M. R. Tan, W. W. Tjiu, X. Y. Ling, *Small* **2016**, *12*, 4531.
[42] S. Pedireddy, H. K. Lee, W. W. Tjiu, I. Y. Phang, H. R. Tan, S. Q. Chua, C. Troadec, X. Y. Ling, *Nat. Commun.* **2014**, *5*, 4947.
[43] T. Fujita, P. F. Guan, K. McKenna, X. Y. Lang, A. Hirata, L. Zhang, T. Tokunaga, S. Arai, Y. Yamamoto, N. Tanaka, Y. Ishikawa, N. Asao, Y. Yamamoto, J. Erlebacher, M. W. Chen, *Nat. Mater.* **2012**, *11*, 775.
[44] H. Lv, D. D. Xu, J. Henzie, J. Feng, A. Lopes, *Chem. Sci.* **2019**, *10*, 6423.
[45] H. Lv, D. D. Xu, L. Z. Sun, B. Liu, *J. Phys. Chem. Lett.* **2020**, *11*, 5777.
[46] L. W. Li, H. J. You, L. J. Zhao, R. Y. Zhang, M. U. Amin, J. X. Fang, *J. Phys. Chem. Lett.* **2021**, *12*, 5271.
[47] Y. Sun, L. Zhuang, J. Lu, X. Hong, P. Liu, *J. Am. Chem. Soc.* **2007**, *129*, 15465.
[48] V. R. Stamenkovic, B. Fowler, B. S. Mun, G. F. Wang, P. N. Ross, C. A. Lucas, N. M. Markovic, *Science* **2007**, *315*, 493.
[49] B. Lin, G. Yang, L. Wang, *Angew. Chem. Int. Ed.* **2019**, *58*, 4587.
[50] B. N. Zope, D. D. Hibbitts, M. Neurock, R. J. Davis, *Science* **2010**, *330*, 74.
[51] F. Tao, M. E. Grass, Y. W. Zhang, D. R. Butcher, J. R. Renzas, Z. Liu, J. Y. Chung, B. S. Mun, M. Salmeron, G. A. Somorjai, *Science* **2008**, *322*, 932.
[52] F. Tao, M. E. Grass, Y. W. Zhang, D. R. Butcher, F. Aksoy, S. Aloni, V. Altoe, S. Alayoglu, J. R. Renzas, C. K. Tsung, Z. W. Zhu, Z. Liu, M. Salmeron, G. A. Somorjai, *J. Am. Chem. Soc.* **2010**, *132*, 8697.

